

Article

Discovery of Pseudomorph Scapolite and Diagenetic Indication from the Permian Volcaniclastic Rocks in Western Sichuan (SW China)

Xiaohong Liu ^{1,*} , Yue'e Li ¹ , Cong Tan ², Zhenglin Cao ², Hui Jin ², Mingyou Feng ¹ , Maolong Xia ³ and Junlang Chen ¹

¹ School of Geoscience and Technology, Southwest Petroleum University, Chengdu 610500, China; fmyswpu@163.com (M.F.)

² Research Institute of Petroleum Exploration and Development, PetroChina, Beijing 100083, China

³ Exploration and Development Research Institute, PetroChina Southwest Oil & Gas Field Company, Chengdu 610041, China

* Correspondence: liuxiaohong_swpu@163.com

Abstract: Volcaniclastic rocks are important unconventional oil and gas reservoirs from which it is difficult to determine the protolith due to strong metasomatic alteration. Intensive alteration has occurred in much of western China, but few robustly documented examples are known from which to assess the alteration processes. Further recognition from the petrological and mineralogical record is essential to quantify the diagenetic environment, the degree of alteration, and its impacts. Permian volcanic rocks are widely developed in the western Sichuan Basin (southwestern China), with a thickness of more than 200 m. The thickness of volcaniclastic rocks in the Permian Emeishan Basalt Formation is up to 140 m, with a 5600~6000 m burial depth. In this study, we demonstrate an approach to recognizing hydrothermal alteration by the occurrence of scapolite megacryst mineral pseudomorphs (SMMPs) in Permian volcaniclastic rocks in the Sichuan Basin (southwestern China). The results show that SMMPs in the Permian volcaniclastic rocks in the western Sichuan Basin mainly occur in the lower part of the Permian basalts as intragranular minerals and rock inclusions. Scapolite is transformed into quartz and albite, and only the pseudomorph is preserved, indicating secondary hydrothermal fluid metasomatic alteration. Scapolite is formed after microcrystalline titanite and is the product of the high-temperature pneumatolytic metasomatism of plagioclase from the mafic protolith during the post-magmatic stage. The mixing of meteoric water and barium-rich hydrothermal fluid leads to the precipitation of barite; additionally, the pores are filled with barite and halite after the alteration of scapolite. The silicification and hydrothermal dissolution of scapolite and the albitization of sodium-rich matrix minerals increase the pore volume, which is conducive to the later recharge by hydrothermal fluids. The discovery of SMMPs can serve as an indicator of the high-temperature pneumatolytic metasomatism and mixing of meteoric water and deep hydrothermal fluid.

Keywords: Sichuan basin; southwestern China; Permian volcaniclastic rock reservoir; scapolite megacryst mineral pseudomorphs; pneumatolytic metasomatism



Citation: Liu, X.; Li, Y.; Tan, C.; Cao, Z.; Jin, H.; Feng, M.; Xia, M.; Chen, J. Discovery of Pseudomorph Scapolite and Diagenetic Indication from the Permian Volcaniclastic Rocks in Western Sichuan (SW China). *Minerals* **2024**, *14*, 200. <https://doi.org/10.3390/min14020200>

Academic Editor: Georgia Pe-Piper

Received: 31 October 2023

Revised: 12 February 2024

Accepted: 13 February 2024

Published: 15 February 2024



Copyright: © 2024 by the authors. Licensee MDPI, Basel, Switzerland. This article is an open access article distributed under the terms and conditions of the Creative Commons Attribution (CC BY) license (<https://creativecommons.org/licenses/by/4.0/>).

1. Introduction

Volcanic rocks are important unconventional reservoirs with a wide distribution [1–4]. Among them, volcaniclastic rocks (especially tuff) have drawn significant attention from the oil and gas exploration community; tight oil resources have been found in low-permeability tuff reservoirs in many oil- and gas-bearing basins [5]. In addition, tuff has specific features such as, a small particle size, complex alteration pathway, and intricate reservoir space, making it difficult to study volcaniclastic rocks [6–8].

Volcanic rocks, particularly volcanoclastic rocks, are prone to weathering and hydrothermal alteration; temperature, pressure, and hydrothermal fluid composition are key parameters. Alteration not only changes the mineralogical composition and structure of the primary rocks, but also changes their geochemical characteristics [9–11]. Some studies have suggested that the geochemical characteristics of volcanic rock minerals are not always significantly changed during the process of alteration. For example, in the case of the hydrothermal alteration of rhyolite, the geochemical characteristics of the new minerals are not significantly different from those of primary rocks [12]; for example, the heavy rare-earth element (HREE) contents of whole rocks in the Sm-Nd isotopic system remained consistent in the Lala Fe-Cu-REE deposit [13]. Generally, however, alteration changes the characteristics of protoliths. During hydrothermal alteration, the concentration of aluminum, iron, manganese, and magnesium in a hydrothermal solution gradually decreases, while the concentration of calcium gradually increases, and carbonate minerals are formed [14,15]. The alteration minerals in basalts are mainly chlorite, quartz, montmorillonite, calcite, zeolite, and pyrite [14–16]. Moreover, apatite mineral chemistry studies show an enrichment in light rare earth elements (LREEs) and negative Eu anomalies via hydrothermal alteration [17]. Tuff alteration also changes the geochemical characteristics of primary rocks [18]. Furthermore, in the process of mineral alteration, changes in mineralogy affect the density and volume of rocks. More specifically, changing the volume of surrounding rocks affects the seal integrity of fractures, further impacting the physical properties of volcanic rock reservoirs [19]. Some mineral alteration leads to an increase in the surrounding rock volume, which blocks fluid conduits and hinders further reactions. For example, the presence of chlorite [20] and the precipitation of quartz [11] lead to a decrease in rock density and an increase in rock volume, greatly reducing the porosity and permeability of the reservoir. Conversely, feldspar sericitization (clay alteration) is an alteration process that reduces volume, creates reservoir space, and improves the reservoir properties [18,21].

Permian volcanic rocks are widely distributed in the western Sichuan Basin (southwestern China), with a thickness of more than 200 m, and have great exploration potential. Among them, the volcanoclastic rocks in the Chengdu–Jianyang area on the northern margin of the Emeishan Large Igneous Province (EMLP) are widely distributed. The thickness of volcanoclastic rocks in the Permian Emeishan Basalt Formation is up to 140 m, with a 5600–6000 m burial depth [22–25]. Previous studies have indicated that the effects of the volcanic environment, lithofacies, reservoir physical properties, and diagenesis on volcanoclastic rocks are crucial [24]. Shimizu (2021) and Somarin and Lentz (2008) showed that the formation of new minerals via alteration can provide information regarding the diagenetic environment. For example, quartz, pyrite, epidote, chlorite, and calcite often occur in low-temperature hydrothermal systems [26,27]. However, it is often difficult to determine the lithology of the protolith due to strong metasomatic alteration, which further affects the analysis of its genetic mechanism [7,28–30]. In addition, the effect of metasomatic alteration on the reservoir can be very important, in which minerals maintain their original crystal morphology. Therefore, it is helpful to analyze the composition of primary and alteration minerals, identify the lithology of protoliths, and reconstruct fluid–rock interactions under the condition of strong alteration according to the pseudomorphic characteristics and chemical composition changes in metasomatic minerals [31,32]. In this study, our main objectives were to (1) specify the timing and the process of scapolitization, (2) propose a conceptual model of hydrothermal alteration, and (3) investigate the origin of scapolite.

2. Geological Setting

The western Sichuan Basin (southwestern China), located in the western region of the Yangtze paraplatform (Figure 1a), is a composite superimposed basin with multi-cycle evolution [33]. This basin is a late Mesozoic–Cenozoic foreland basin overlying a Precambrian–Middle Mesozoic passive margin [34] that experienced strong compressive tectonic deformation after the Permian. During the Jinning tectonic activity and Chengjiang

tectonic activity, the basement structure was established and separated by a central uplift of brittle lithologies [35]. Thereafter, the basin experienced several significant tectonic episodes, including the Tongwan, Caledonian, Yunnan, Dongwu, Indosinian, Yanshanian, and Himalayan [36,37]. The study area (Jianyang) is located in the western Sichuan Basin, which is situated on the border of Chengdu and Suining counties (Figure 1a,b), restricted by the Longquanshan Fault. The Permian Emeishan Basalt Formation lies within the eastern part of the Emeishan Large Igneous Province, which developed as a result of Hercynian orogeny and ranges in age from 261 to 257 Ma [38].

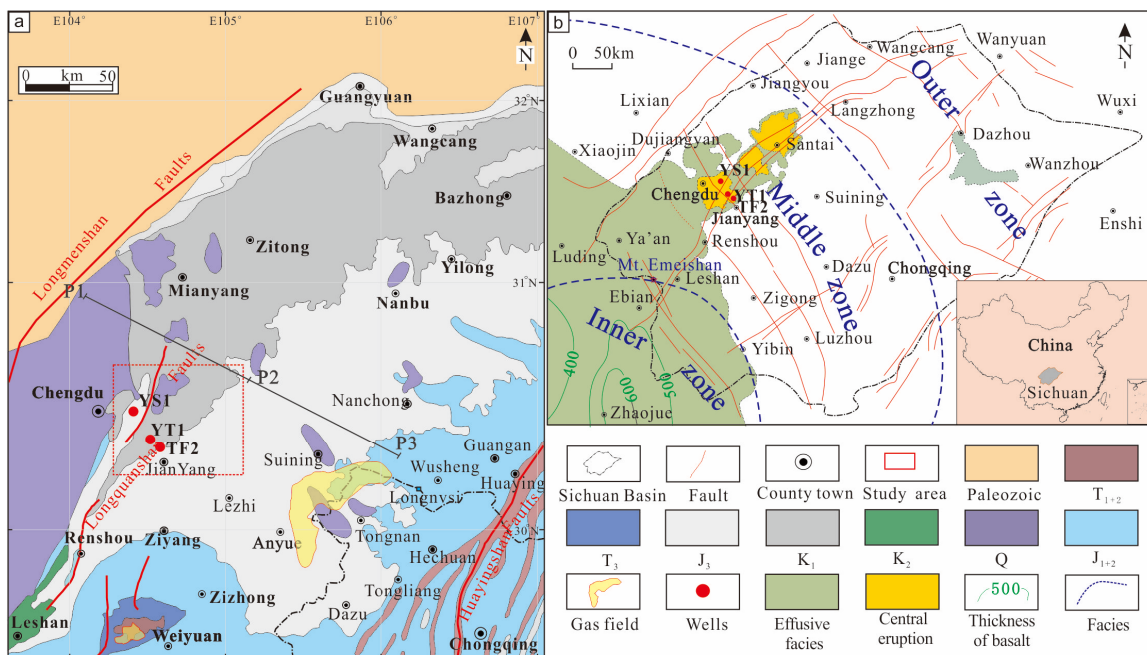


Figure 1. Simplified geological maps and location of Sichuan Basin. (a) Simplified geological map in the western Sichuan Basin, southwest China; (b) Distribution map of Permian volcanic rocks facies in Sichuan basin [39]. Red dotted box is the study area and YS1, YT1, TF2 are the exploratory wells. P1, P2, P3 are the locations corresponding to Figure 2a.

Emeishan basalt is widely distributed in the western and southwestern Sichuan Basin, and has an exposed area greater than $25 \times 10^4 \text{ km}^2$ [40]. Volcanic rocks comprise the main continental eruption, and partly interbedded volcanic rocks and limestone indicate a marine eruption in the early stage [39,41]. The thickness of the Emeishan Basalt Formation ($P_2\beta$) in the southwestern Sichuan Basin is up to 1400 m, with a 500–6000 m burial depth, and at least eight eruptive cycles are recognized [42]. Unconformable contacts lie between the Emeishan Basalt Formation ($P_2\beta$) and the underlying Middle Permian Maokou Formation (P_2m) and the overlying Permian Longtan Formation (P_2l). The underlying Maokou Formation interval is mainly composed of gray thin-to-medium limestone with thin dark calcareous mudstone interlayers, representing a relatively shallow and mid-energy marine environment during the sea-level fall. The upper part of the Maokou Formation was mostly eroded during the Dongwu movement. The overlying Longtan Formation interval is mainly composed of black thin mudstone and silty mudstone, locally containing carbonaceous shale and coal, which belong to the coastal marsh facies. The Longtan Formation comprises subordinate source rocks for oil and gas exploration, whilst Cambrian shales are primary source rocks [42].

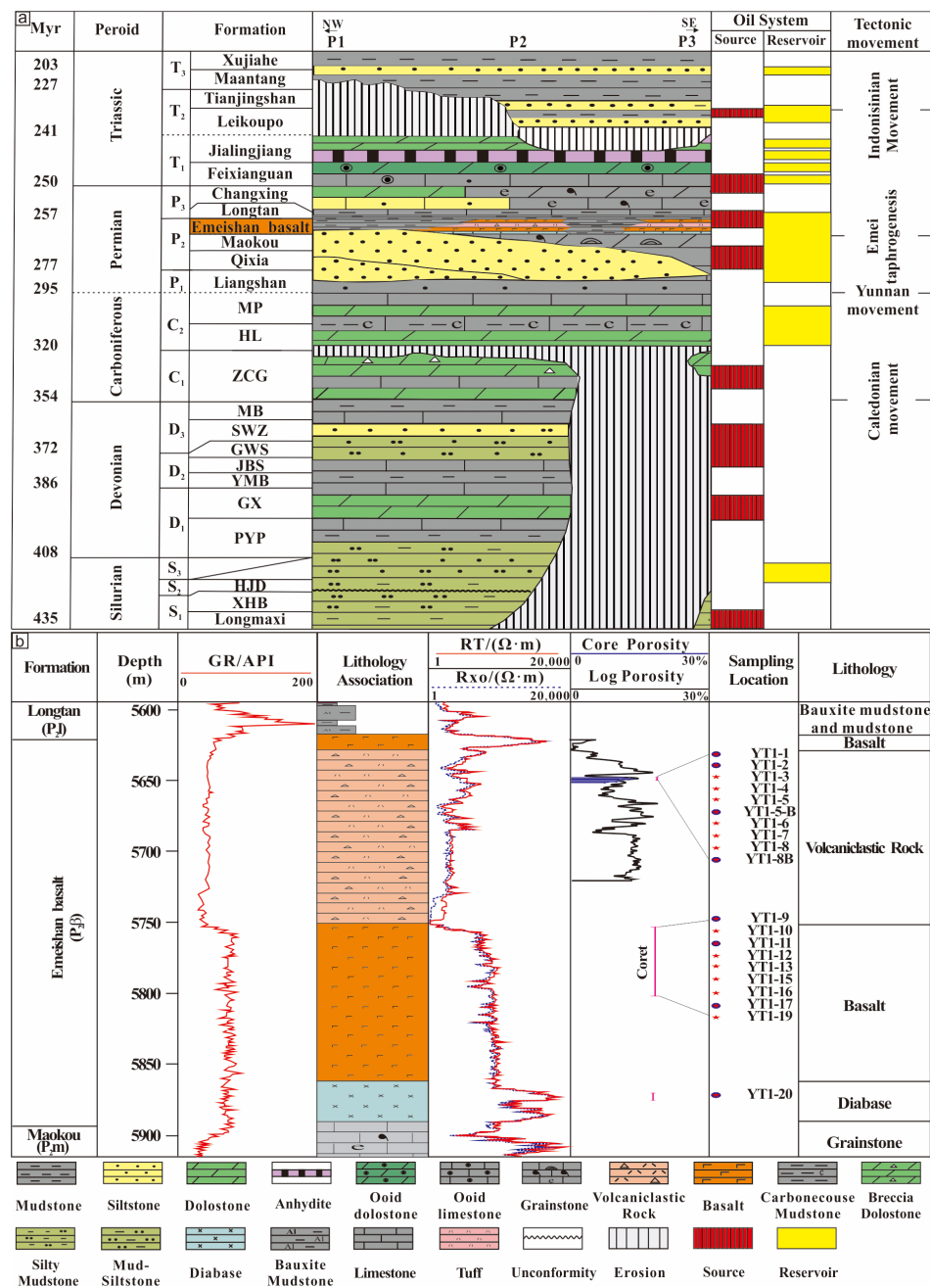


Figure 2. Comprehensive histogram of Sichuan Basin. (a) Comprehensive histogram of stratigraphy along the NW-SE section across western and central part of Sichuan Basin; (b) stratigraphic column of Permian in Jianyang area (western Sichuan). Line P1–P3 corresponds to Figure 1a.

Several wells (YS1, YT1, TF2) have been drilled into the Permian Emeishan basalt interval in the Jianyang area of the western Sichuan Basin. Well YT1, located in the Jianyang area of the western Sichuan Basin, is the first key risk exploration well in the Permian volcaniclastic rock reservoir and produced 225,000 m³/d of gas during the test. Previous studies have shown that the distribution of the volcaniclastic rocks in well YT1 is obviously controlled by the Longquanshan basement fault (Figure 1a). The volcaniclastic rock section has a thickness of almost 100 m and consists of deposits of alkaline basalt rock fragments (Figure 2a,b). It is widely recognized that the reservoir space type is dominated by secondary nano-micropores, and the volcanic reservoir is a high-quality porous natural gas reservoir [22,41,43–45]. It is also recognized that the volcanic eruption environment, lithology, and lithofacies are the basis for the formation of volcaniclastic rock

reservoirs, while a series of alteration processes that volcanic rocks undergo when they condense are the key factors for the formation of reservoirs [46,47]. The alteration processes include hydrothermal alteration, weathering, and burial dissolution. Notably, a series of actions related to hydrothermal fluid activities contribute greatly to the formation of reservoir pore space. In addition, the hydrothermal fluid activities also formed particular mineral paragenesis assemblages, e.g., the hydrothermal accessory minerals chlorite and albite [39,46].

Some hydrothermal accessory minerals such as titanite, apatite, monazite, and zircon can be found in the upper part of the volcanoclastic rocks (5645.76–5646.25 m). A unique altered form of the mineral scapolite, referred to as scapolite megacryst mineral pseudomorphs (SMMPs), can also be found. SMMPs occur as large and elongated crystal forms, with lengths ranging from 1 to 5 cm, and belong to the megacryst–pegmatitic mineral group. This alteration pseudomorph is blue-gray in hand specimens (Figure 3a–d) and colorless and transparent in thin sections. It is composed of quartz, albite, titanite, calcite, barite, and chlorite. Additionally, secondary minerals such as tourmaline and anthophyllite are found in the lower part of volcanoclastic rock sections.

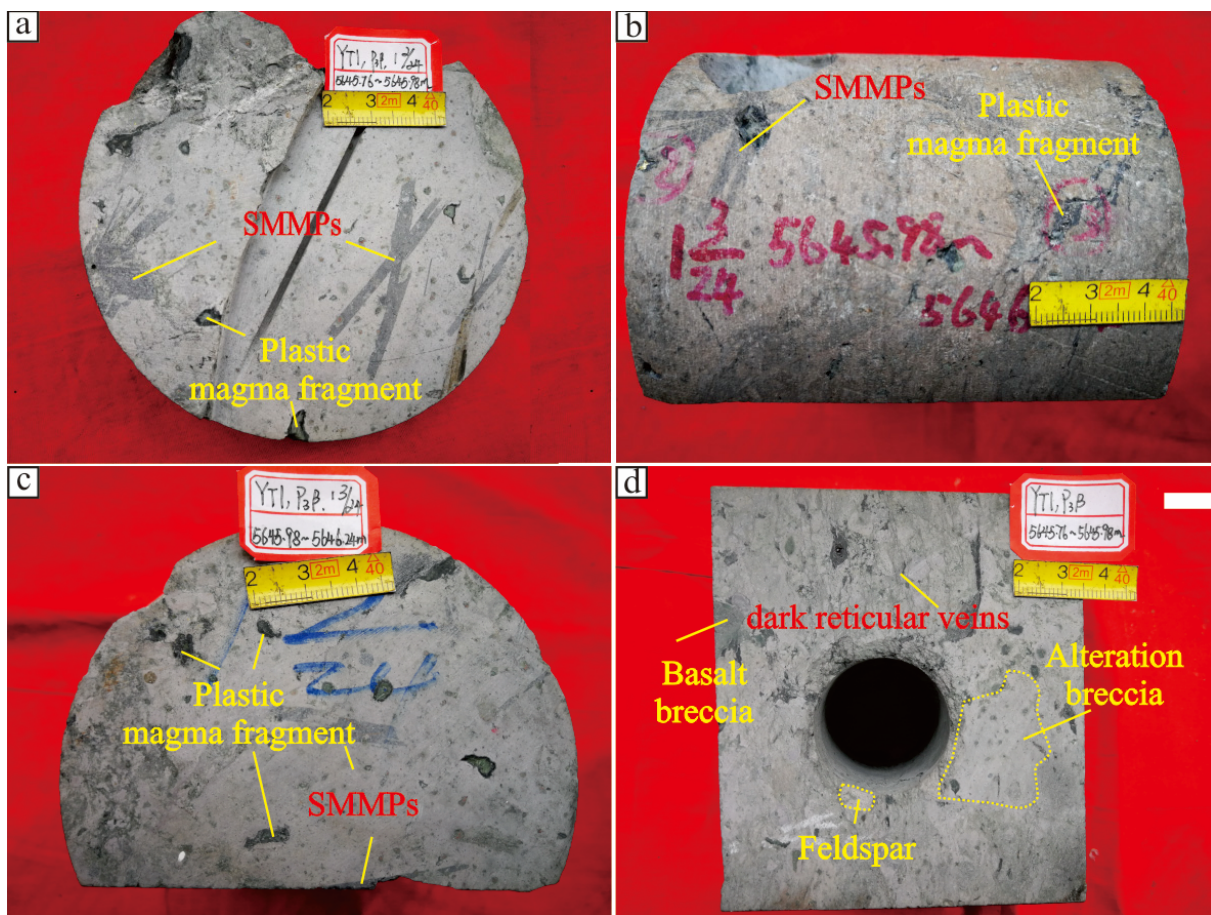


Figure 3. Core photographs of scapolite megacrysts minerals pseudomorph (SMMPs) in volcanoclastic rocks from the Permian Formation. (a) Breccia lava with plastic magma fragment and scapolite giant crystal pseudomorph, YT1 well, 5645.76–5645.98 m; (b) Breccia lava with plastic magma fragments and SMMPs, YT1 well, 5645.98–5646.24 m; (c) Breccia lava with plastic magma fragments and SMMPs, YT1 well, 5645.98–5645.24 m; (d) Breccia lava with feldspar pieces, basalt breccia, altered breccia and dark reticular veins, YT1 well, 5645.76–5645.98 m.

3. Sampling and Methodology

Twenty cores from well YT1 and four cores from well TF2 were collected in order to document the petrological characteristics of the volcanic rocks. One hundred doubly polished and blue epoxy-impregnated thin sections were produced to determine lithological components, porosity, and alteration minerals. Four samples were prepared for fluid inclusion analysis. Thin-section, electron probe, and fluid inclusion investigations were all carried out at the Natural Gas Geology Key Laboratory of Sichuan Province, Southwest Petroleum University, China. Firstly, the rock was ground into 0.03 mm thin sections, and these were examined with an Olympus BX53M microscope (Shinjuku-ku, Tokyo Japan, Olympus). Bulk and clay mineral analyses based on X-ray diffraction (two samples) were accomplished at the National Key Laboratory of Oil and Gas Reservoir Geology and Exploitation, Southwest Petroleum University, in which selected samples rich in SMMPs were ground into 200-mesh powder and tested for bulk mineral composition using an X-ray diffractometer (X Pert PRO MPD, PANalytical B.V., Almelo, The Netherlands). Particles smaller than 2 μm were further extracted for separate determination of clay mineral types and contents [48]. The standard minerals were calculated using an Excel (2009) spreadsheet designed by Kurt Hollocher and using the Le Maitre (1976) method to adjust iron oxide according to volcanic rocks. Oxides were converted to 100% after removing H_2O -, etc. The standard minerals were represented by the weight percentage content. Other parameters were as follows: combination index (σ): $\sigma_{43} = (\text{Na}_2\text{O} + \text{K}_2\text{O}) / (\text{SiO}_2 - 43)$ (Wt%); differentiation index (DI) = Qz + Or + Ab + Ne + Lc + Kp. The A/NK-A/CNK diagram of volcanic rocks and the chemical type discrimination were taken from Mania and Piccoli (1989): $A/NK = \text{Al}_2\text{O}_3 / (\text{Na}_2\text{O} + \text{K}_2\text{O})$ (mol); $A/CNK = \text{Al}_2\text{O}_3 / (\text{CaO} + \text{Na}_2\text{O} + \text{K}_2\text{O})$ (mol); and alkalinity rate (AR) = $[\text{Al}_2\text{O}_3 + \text{CaO} + (\text{Na}_2\text{O} + \text{K}_2\text{O})] / [\text{Al}_2\text{O}_3 + \text{CaO} - (\text{Na}_2\text{O} + \text{K}_2\text{O})]$ (Wt.%).

Electron probe microanalyzer (EPMA) analysis (YT1 well, 5645.76 m, 5645.98 m, 5646.41 m) was carried out on polished sections 500 μm thick that were cut from the same blocks as thin sections. EPMA analyses were performed using a JXA-8230 electron probe micro-analyzer (Showima, Tokyo, Japan, JEOL) combined with a backscattered electron (BSE) detector, energy spectrometer (EDS) and wavelength dispersive spectrometer (WDS) (London, UK, Oxford Instruments). The accelerating voltage was 15.0 kV, the beam current was 20 nA, the beam diameter was 5 μm , and the peak counting time was 10 s. The spectral analysis accuracy was better than 1% (main element content > 5%) and 5% (secondary element content 1%–5%); the detection limit was 0.01 wt.%. EDS surface scanning was used to scan the local area of the scapolite and obtain the distribution of nine main elements: Si, Al, K, Na, Ba, Ca, Ti, Fe, and Mg. Authigenic minerals and micropores were observed using a Quanta 650 FEG scanning electron microscope (SEM) (Brno-Kralovo Pole, Czech Rep, FEI Czech Republic S.R.O) with backscatter electron (BSE) imaging in the State Key Laboratory of the Southwest Petroleum University.

Fluid inclusion was investigated at the Southwest Petroleum University with a Linkam THMSG600 system (Salfords, Surrey, UK, Linkam Scientific Instruments). The composition of the fluid inclusion was measured using a Renishaw inVia-Qontor microconfocal Raman spectrometer (Waltham, MA, US, America Thermo Scientific) laser with a wavelength of 532 nm and a grating size of 1800 L/mm. The exposure time was 2 s, laser power was 10%, and accumulation number was 3. The measurement range of the hot and cold stage was $-196\sim 600$ $^\circ\text{C}$, and the heating–freezing rate was reduced to 1–10 $^\circ\text{C}/\text{min}$. When the temperature was close to the phase transition temperature, the heating–freezing rate was reduced to 0.2–1 $^\circ\text{C}$. During the cooling process, the measurement accuracy was ± 0.1 $^\circ\text{C}$ when the temperature was less than 30 $^\circ\text{C}$, and the measurement accuracy was ± 1 $^\circ\text{C}$ when the temperature was between 30 $^\circ\text{C}$ and 300 $^\circ\text{C}$. The analysis was carried out in the laboratory at room temperature (25 $^\circ\text{C}$) and 50% humidity.

4. Results

4.1. Petrology and Mineralogy

The core observation results show that SMMPs mainly occur at a depth of 5645.76–5745.98 m in well YT1 (also an important reservoir interval), consisting mainly of breccia lava. In addition to SMMPs, there are basaltic and other intermediate-basic rock fragments, plastic magma fragments, plastic rock debris, and feldspar crystal fragments (Figure 3a–d). The rock samples display a massive structure and common dark mineral network veinlets, likely corresponding to fluid migration conduits (Figure 3d). According to the results of the major and trace element analyses, the SiO₂ content ranges from 51.5 to 57.1 wt.%, and the Na₂O + K₂O content ranges from 6.7 to 8.9 wt.%. The rock samples belong to the intermediate-basic alkaline igneous rock series. The Chemical Index of Alteration (CIA) ranges from 58.1 to 59.3, Alteration index (AI) ranges from 9.56 to 17.29, and Loss on ignition (LOI) ranges from 2.01 to 3.27 wt.% (Table 1) [49,50]. The TiO₂ content ranges from 4.2 to 4.4 wt.%, the Sr content ranges from 129 to 141 ppm, and the Ba content ranges from 35.5 to 49.2 ppm; the Sr/Ba ratio ranges from 2.87 to 3.63 (Table 1). The total rare earth element content (ΣREE) ranges from 202.95 to 320.32 ppm, and LREE/HREE ranges from 6.96 to 8.86 (Table 2) [39]. The X-ray diffraction analyses show that albite and chlorite are the most abundant minerals, together constituting more than 90 wt.% of the rocks. Quartz and titanite are the other two important minerals but are present in low concentrations, from 1 to 3 wt.% and from 5 to 7 wt.%, respectively (Figure 4).

The CIPW normative composition calculated for rock samples (Table 3) includes albite (75.80 wt.%), anorthite (7.09%), titanite (2.85 wt.%), diopside (2.24 wt.%), and iron-rich minerals such as ilmenite (5.91 wt.%) and hematite (2.79 wt.%). However, XRD did not detect minerals such as Ca-rich plagioclase, diopside, ilmenite, and hematite. The minerals consist of alteration minerals and primarily include albite, titanite, and chlorite, subordinated by quartz (<1 wt.%), indicating a very high degree of alteration (Figure 4).

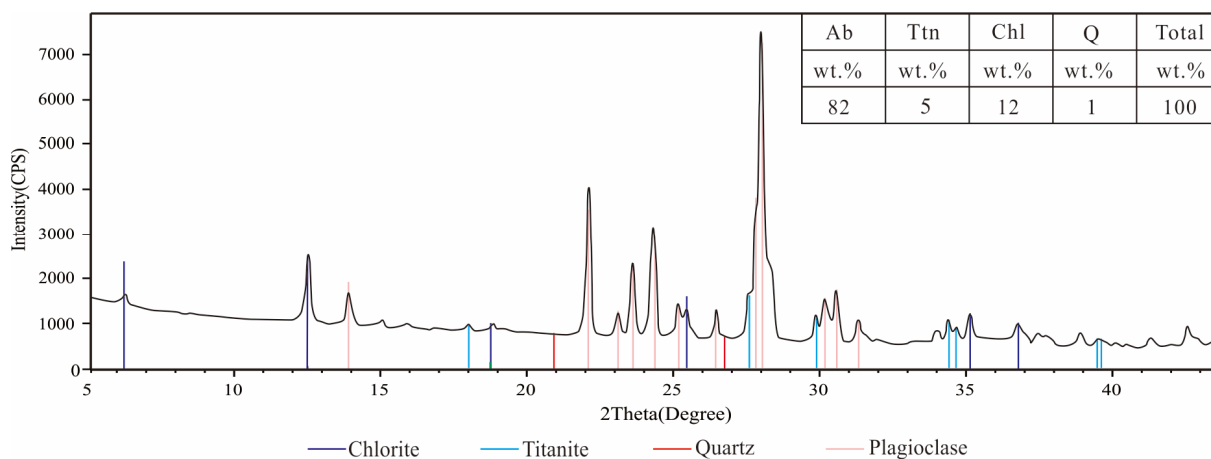


Figure 4. X-ray diffraction analysis results of volcaniclastic rocks from the Permian Formation, Well YT1; 5645.98m; Detect limitation: 1%. Ab-Albite; Ttn-titanite; Chl-Chlorite; Q-Quartz.

Table 1. The major and trace element analysis of Permian volcaniclastic rocks in well YT1.

Sample Number	Depth m	Al ₂ O ₃	CaO	K ₂ O	BaO	SrO	Na ₂ O	SiO ₂	MgO	Sr	Ba	Sr/Ba	LOI	CIA	AI
		wt. %	wt. %	wt. %	wt. %	wt. %	wt. %	wt. %	wt. %	ppm	ppm				
YT1-1	5645.76	16.02	4.24	0.07	0.03	0.02	6.67	51.09	2.21	129.0	35.5	3.63	3.27	63.91	17.29
YT1-3	5645.98	17.03	3.41	0.07	0.04	0.02	8.80	57.09	1.22	141.0	49.2	2.87	2.01	61.61	9.56

LOI- Loss on ignition; AI-alteration index; CIA-chemical index of alteration.

Table 2. The REE contents of Permian volcanoclastic rocks in well YT1.

Sample Number	Depth m	La	Ce	Pr	LREE							HREE					Σ LREE ppm	Σ HREE ppm	Σ REE	LREE/HREE
					Nd	Sm	Eu	Gd	Tb	Dy	Ho	Er	Tm	Yb	Lu					
YT1-1	5645.76	54.7	131.5	16.35	66.7	14.5	4.09	12.25	1.71	8.59	1.64	4.11	0.55	3.18	0.45	287.84	32.48	320.32	8.86	
YT1-3	5645.98	22.9	81.6	11.33	47.8	10.65	3.18	9.44	1.34	7.03	1.28	3.27	0.44	2.36	0.33	177.46	25.49	202.95	6.96	

Table 3. CIPW results of volcanoclastic rocks from the Permian Formation, well YT1, 5645.98 m.

CIPW Calculation Mineral (Matrix)	Q	An	Ab	Or	Di	Hy	Ol	Il	Hm	Ap	Zr	Cm	Ttn	Th	Total
	wt.%	wt.%	wt.%	wt.%	wt.%	wt.%	wt.%	wt.%	wt.%	wt.%	wt.%	wt.%	wt.%	wt.%	wt.%
	0.0	7.09	75.78	0.42	2.24	0.49	1.11	5.91	2.79	1.18	0.07	0.02	2.85	0.09	100.04
	DI = 76.2		H ₂ O = 1.25		A/NK = 1.17		A/CNK = 0.821			AR = 2.53			$\sigma_{43} = 5.35$		

Above data is calculated from the major and trace element of matrix component (Table 1) (YT1-3, 5645.98 m). Q-Quartz; An-Anorthite; Ab-Albite; Or-Orthoclase; Di-Diopside; Hy-Hypersthene; Ol-Olivine; Il-Ilmenite; Hm-Hematite; Ap-Apatite; Zr-Zircon; Cm-Chromite; Ttn-Titanite; Th-Thenardite; Chl-Chlorite.

Dark reticular veins are composed of subhedral to anhedral microcrystals of titanite; the enclosed breccia is characterized by directional features that obviously indicate flow. Additionally, hematite fills the dark mineral dissolution pores (Figure 5a). The SMMPs are mainly subhedral and bypass or locally transect the titanite veins, indicating that the pseudomorphs formed slightly later than the titanite (Figure 5b). The SMMPs could have two possible origins: (1) replacement of scapolite by quartz, albite, titanite, barite, calcite, and chlorite; (2) complete dissolution of scapolite, the generated pores being filled later by the same secondary minerals (Figure 5c,d). Further, hornblende, calcium-rich plagioclase (dissolved tabular albite, titanite, and reprecipitated), basalt (Figure 5c,f), and other minerals or rock inclusions are clearly visible (Figure 5e,f).

Metasomatic alteration of the scapolite produced and formed much of the quartz, and there are few quartz crystals in the matrix (Figure 5c,f). Quartz is suggested to mainly result from the interaction between the fluid and the scapolite. In addition, amygdaloidal structures present in the altered rock are filled with albite (Figure 5d).

Moreover, xenomorphic granular barite is present between quartz and other minerals. In the electron probe backscattering image, barite can be distinguished from other minerals with higher brightness; the rim is often enclosed by subhedral and euhedral granular quartz, and there may be a small amount of lath albite mineral inclusions inside (Figure 6a,b). Barite is almost invisible in the matrix, except that it is present inside and outside the scapolite crystal, suggesting that the precursor is derived from the decomposition products of scapolite minerals.

The matrix is mainly composed of albite, microcrystalline titanite, and chlorite. Microporosity in the matrix is abundant and is associated with volcanic glass devitrification (Figure 7a–c). In addition, euhedral granular halite crystals fill the matrix pores (Figure 7d).

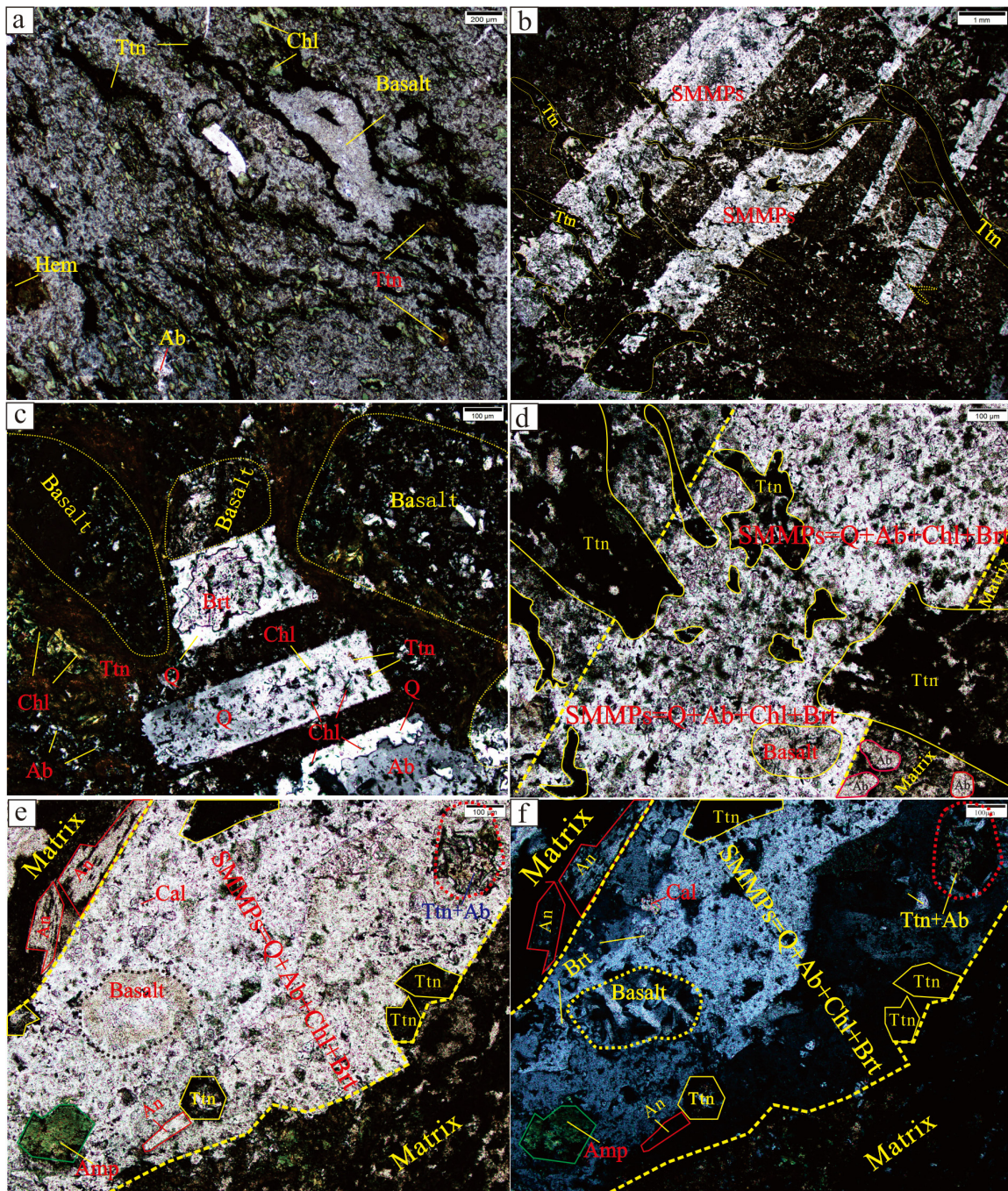


Figure 5. Photomicrographs of the Permian volcanoclastic rocks and SMMPs in the western Sichuan Basin. (a) Microcrystalline titanites are arranged in a directional manner around the breccia to form a dark reticular vein, dark mineral dissolution pore in the hematite, well YT1, 5645.76 m, blue casting, plane polarized light; (b) The SMMPs is subhedral, growing around dark mesh veins, well YT1, 5645.98 m, plane polarized light; (c) The scapolite is replaced by quartz and barite, and a chlorite inclusion is also seen, well YT1, 5645.98 m, crossed polarized light; (d) The SMMPs is composed of quartz, albite, chlorite, and barite, and titanites are transected by SMMPs, well YT1, 5645.98 m, plane polarized light, amygdaloidal structures—red circle; (e) Mineral or rock inclusions such as amphibole, plagioclase feldspar (now converted into albite and titanite), and basalt rock fragment are found in the SMMPs that is replaced by quartz, well YT1, 5645.98 m, plane polarized light; (f) Photo (e) crossed polarized light. Scp—Scapolite; Q—Quartz; Ab—Albite; Ttn—Titanite; Brt—barite; Chl—chlorite; Amp—Amphibolite; Hem—Hematite; Cal—Calcite.

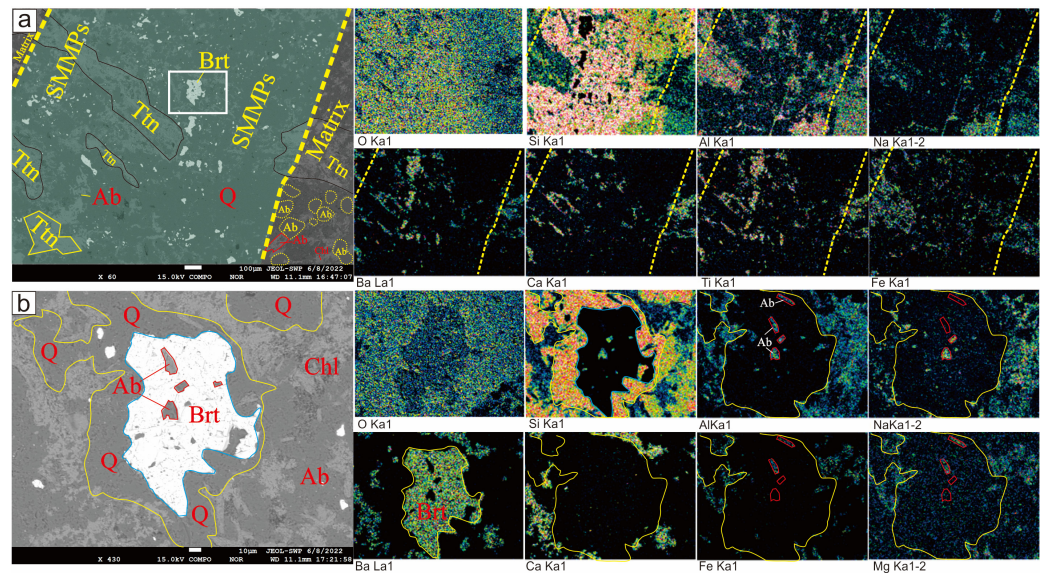


Figure 6. The back-scattered electron image (of EPMA) characteristics of SMMPs. (a) Large number of xenomorphic granular barites, irregular titanite, flaky chlorites, etc. are scattered in the SMMPs composed of quartz minerals, and the matrix is mainly composed of albite with the morphology of analcime and albite after devitrification of volcanic glass. Titanites (black line) are obviously transected by SMMPs, and partly (yellow polygon) remain pseudomorphs of hornblende. The yellow thick dashed line shows the boundary between the matrix and SMMPs. In the matrix, the yellow dotted circles show an amygdaloidal structure filled by albite, and the red polygon shows plagioclase replaced by albite, well YT1, 5645.98 m, the boundary of SMMPs and matrix is clearly visible (dotted yellow line); (b) The enlargement of the area enclosed by the white rectangle in white rectangle in (a), well YT1, 5645.98 m. Q–Quartz; Ab–Albite; Ttn–Titanite; Brt–barite; Chl–Chlorite; O Ka1, Si Ka1, Al Ka1, Na Ka1-2, Ba La1, Ca Ka1, Ti Ka1, Fe Ka1 and Mg Ka1-2 are O, Si, Al, Na, Ba, Ca, Ti, Fe, Mg. The higher the brightness in the image, the higher the element content.

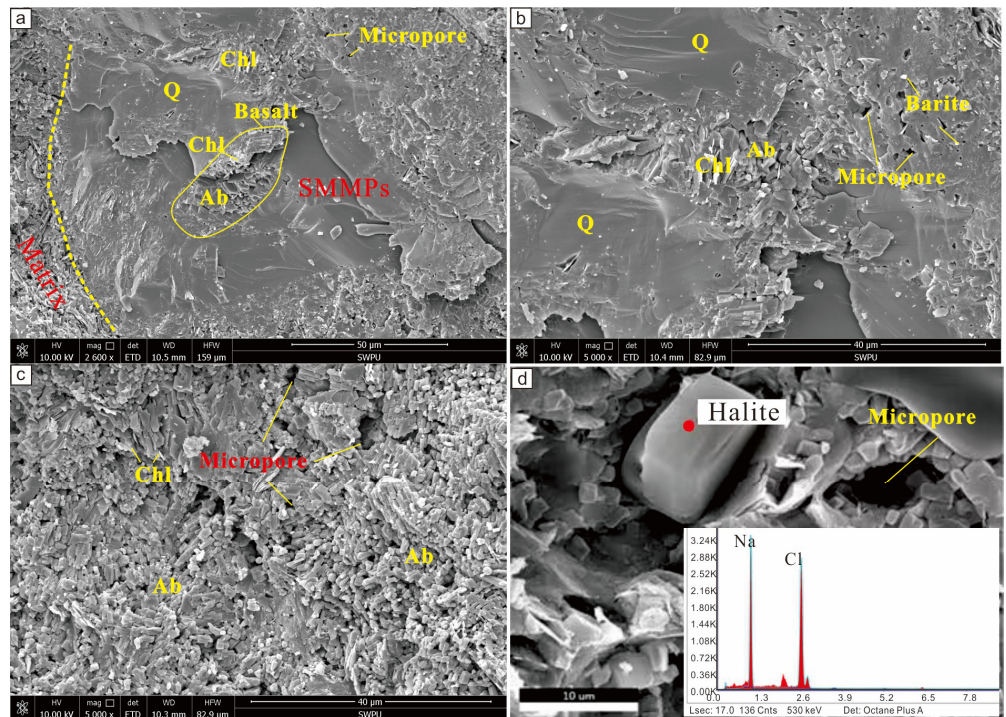


Figure 7. The SEM of the Permian volcanoclastic rocks, well YT1, 5645.98 m. (a) Quartz, chlorite, basalt (yellow line) and albite occur in SMMPs and the boundary of SMMPs and matrix is clearly

visible (dotted yellow line). (b) Quartz, albite, chlorite, barite and micropore occur in SMMPs. (c) Micro-porosity in the matrix is abundant (d) Euhedral granular halite crystals which filling the matrix pores. Q–Quartz; Ab–Albite; Chl–Chlorite.

4.2. Composition of Altered Minerals

The SMMPs formed due to mineral replacement or dissolved-refilling by quartz, albite, titanite, barite, calcite, and chlorite. The electron probe analysis shows that the quartz that replaced scapolite generally contains a small amount of CaO (0.46–1.99 wt.%), FeO (0.09–0.22 wt.%), and Al₂O₃ (0.01–0.07 wt.%) (Table 4). The microcrystalline titanite occurs in bands, and titanite fills the pores resulting from feldspar dissolution; both contain components such as Al₂O₃, ranging from 1.34 to 2.16 wt.%, FeO, ranging from 0.67 to 1.76 wt.%, and BaO, ranging from 0.18 to 0.31 wt.%. However, the pore-filling titanite contains relatively low amounts of TiO₂ and more Al₂O₃ (Table 5). The albite filling the pores and pseudomorph analcime are both pure albite (Ab) with more than 99 wt.% albite, containing only small amounts of orthoclase (Or) and anorthite (An) components (Table 3). The barite generally contains small amounts of components such as SrO, ranging from 2.85 to 3.59 wt.%, FeO, ranging from 0.02 to 0.27 wt.%, and SiO₂, ranging from 0.08 to 0.41 wt.%, and thus showing relatively high levels of these substitution elements (Table 6).

Table 4. The EPMA data of silicate minerals in SMMPs in the Well YT1.

Sample Number	Depth m	SiO ₂ wt.%	TiO ₂ wt.%	Al ₂ O ₃ wt.%	FeO wt.%	Cr ₂ O ₃ wt.%	MnO wt.%	MgO wt.%	CaO wt.%	Na ₂ O wt.%	K ₂ O wt.%	BaO wt.%	Total wt.%	Sample Points	Mineral
YT1-1-A	5645.76	99.29	0.00	0.04	0.10	0.02	0.00	0.00	0.63	0.02	0.00	0.00	100.10	Q-1	MQ
YT1-1-B	5645.76	98.65	0.02	0.06	0.09	0.00	0.00	0.01	1.23	0.00	0.03	0.00	100.09	Q-2	MQ
YT1-3-C	5645.98	99.79	0.00	0.04	0.15	0.02	0.01	0.00	0.46	0.01	0.00	0.00	100.49	Q-3	MQ
YT1-3-D	5645.98	97.70	0.06	0.01	0.17	0.00	0.02	0.00	1.89	0.03	0.00	0.00	99.87	Q-4	MQ
YT1-4-E	5646.41	99.94	0.05	0.07	0.22	0.03	0.00	0.00	0.46	0.05	0.00	0.00	100.82	Q-5	MQ
YT1-4-F	5646.41	97.43	0.00	0.01	0.15	0.01	0.00	0.01	1.99	0.00	0.00	0.00	99.60	Q-6	MQ
YT1-4-G	5646.41	69.58	0.00	19.68	0.04	0.03	0.00	0.00	0.03	11.70	0.09	0.00	101.15	Ab1-1	MA(Ab = 99.36)
YT1-1-H	5645.76	67.19	0.03	19.06	0.07	0.05	0.01	0.01	0.05	12.16	0.08	0.00	98.70	Ab1-2	MA(Ab = 99.34)
YT1-3-I	5645.98	69.43	0.00	19.58	0.06	0.05	0.02	0.00	0.05	11.77	0.09	0.00	101.05	Ab1-3	MA(Ab = 99.27)
YT1-4-J	5646.41	67.54	0.01	19.31	0.08	0.04	0.01	0.02	0.09	12.13	0.07	0.00	99.29	Ab2-1	EA(Ab = 99.25)
YT1-4-K	5646.41	68.70	0.06	19.71	0.08	0.14	0.01	0.02	0.07	12.09	0.07	0.00	100.96	Ab2-2	EA(Ab = 99.32)
YT1-4-L	5646.41	68.40	0.03	19.30	0.02	0.09	0.00	0.00	0.05	11.84	0.06	0.00	99.78	Ab2-3	EA(Ab = 99.44)
YT1-4-M	5646.41	68.08	0.00	19.61	0.03	0.11	0.00	0.01	0.03	12.37	0.06	0.00	100.30	Ab2-4	EA(Ab = 99.58)

Q–Quartz; Ab–Albite; MQ–metasomatic quartz; MA–metasomatic albite; EA–euhedral albite.

Table 5. The EPMA data of titanite in the Well YT1.

Sample Number	Depth m	SiO ₂ wt.%	TiO ₂ wt.%	CaO wt.%	Al ₂ O ₃ wt.%	FeO wt.%	F wt.%	Cr ₂ O ₃ wt.%	Na ₂ O wt.%	BaO wt.%	K ₂ O wt.%	MgO wt.%	Total wt.%	Sample Points	Mineral
YT1-1-Q	5645.76	31.56	34.67	27.85	2.16	1.74	0.34	0.05	0.10	0.27	0.02	0.02	98.65	Ttn1-1	ET
YT1-1-R	5645.76	31.49	34.79	28.00	2.09	1.76	0.44	0.05	0.09	0.29	0.00	0.02	98.84	Ttn1-2	ET
YT1-3-S	5645.98	31.06	36.19	28.08	1.38	1.18	0.47	0.01	0.07	0.18	0.05	0.05	98.71	Ttn2-1	MT
YT1-3-T	5645.98	31.44	37.07	27.37	1.36	0.67	0.25	0.00	0.04	0.29	0.20	0.14	98.82	Ttn2-2	MT
YT1-4-U	5646.41	31.05	36.85	27.33	1.56	1.69	0.27	0.04	0.07	0.31	0.05	0.09	99.33	Ttn2-3	MT
YT1-4-V	5646.41	31.66	36.24	27.77	1.34	0.77	0.37	0.02	0.05	0.27	0.06	0.04	98.58	Ttn2-4	MT

ET–euhedral titanite; MT–microcrystalline titanite.

Table 6. The EPMA data of barite in the Well YT1.

Sample Number	Depth m	BaO wt.%	SO ₃ wt.%	SrO wt.%	Na ₂ O wt.%	K ₂ O wt.%	CaO wt.%	SiO ₂ wt.%	Al ₂ O ₃ wt.%	FeO wt.%	MnO wt.%	MgO wt.%	Total wt.%	Sample Points	Mineral
YT1-1-N	5645.76	59.17	35.23	3.18	0.09	0.02	0.04	0.41	0.07	0.02	0.01	0.00	98.24	Br1-1	barite
YT1-3-O	5645.98	61.18	36.03	2.85	0.14	0.05	0.04	0.33	0.05	0.05	0.04	0.01	100.77	Br1-2	barite
YT1-4-P	5646.41	60.37	35.51	3.59	0.07	0.01	0.24	0.08	0.02	0.27	0.01	0.00	100.14	Br1-3	barite

4.3. Fluid Inclusions

To determine the properties of diagenetic fluids, we measured the homogenization temperatures and freezing temperatures of fluid inclusions in the quartz that replaced the scapolite crystals and analyzed the composition of the fluid. As shown in Figure 8, the fluid inclusions in the quartz mainly occur in isolation, with a round to elliptical shape. The size is between 4 and 6 μm , and these are mainly brine inclusions with a gas–liquid ratio between 5% and 10%. In the area of study, all the fluid inclusions from quartz have homogenization temperatures (T_h) greater than 200 $^{\circ}\text{C}$ (averaging 207 $^{\circ}\text{C}$), and freezing temperatures (T_m ice) ranging from -2 to -1.4 $^{\circ}\text{C}$. The salinities of the fluid inclusions range from 24.1 to 33.9 g/l and are therefore slightly lower than the average salinity of seawater (35 g/l) (Table 7). The results of the homogenization temperatures of the fluid inclusions in quartz are consistent with the formation temperature results calculated from the Si/Al ratio of the chlorite; the temperature of authigenic chlorite is higher than at least 200 $^{\circ}\text{C}$ (even surpassing 300 $^{\circ}\text{C}$) [39,51].

Table 7. Result of microthermometric study of fluid inclusions (average values).

Sample Number	Mineral	Size μm	Vapor Liquid Ratio		FI Type	T_h $^{\circ}\text{C}$	T_m Ice $^{\circ}\text{C}$	Salinity	
			%					g/l	wt.% NaCl eq
YT1-2-A	Quartz	4	10		Pr	210	-1.4	24.1	2.41
YT1-2-B	Quartz	6	6		Pr	205	-1.7	29.0	2.90
YT1-2-C	Quartz	5	5		Pr	208	-1.8	30.6	3.06
YT1-2-D	Quartz	4	8		Pr	205	-2.0	33.9	3.39

Note: Salinity calculation formula according to Bodnar, 1993 [52].

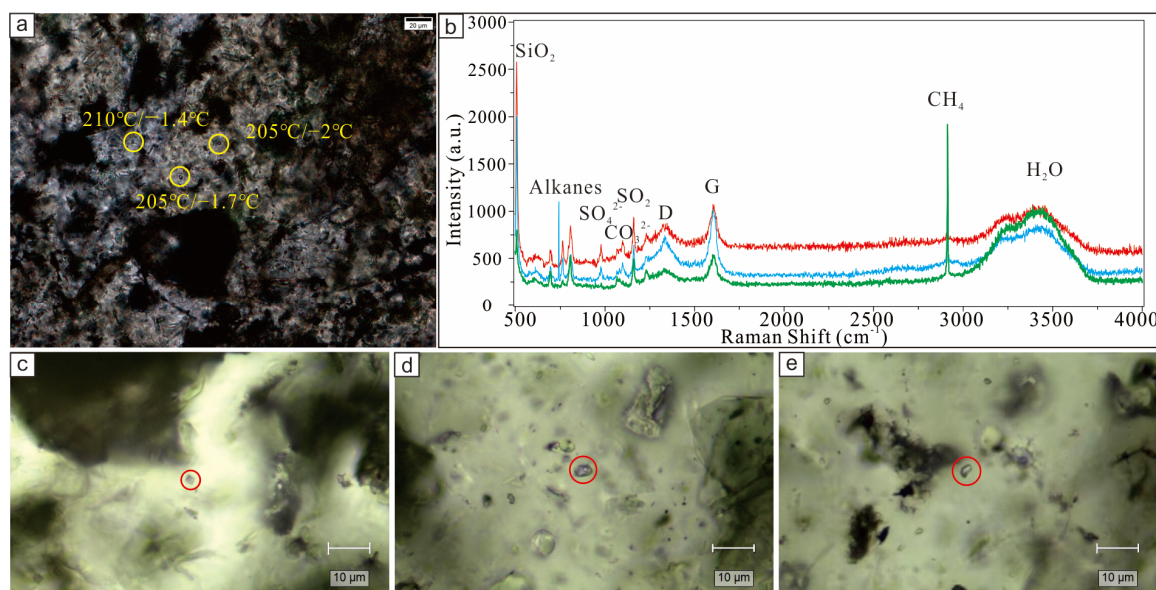


Figure 8. Photomicrographs and laser Raman spectroscopy of fluid inclusions of quartz in the SMMPs. (a) Typical fluid inclusions in quartz; (b) Laser Raman spectroscopy of three fluid inclusions of quartz; (c–e) Typical fluid inclusions in quartz. 5645.76 m. D-Bitumen peak D; G-Bitumen peak G; red circle-fluid inclusion in quartz.

In addition, fluid inclusion components were detected via laser Raman spectroscopy. The test results show that the inclusions not only have distinctive peaks of bitumen, CH_4 , SO_2 , alkanes, and water, but also SO_4^{2-} , CO_3^{2-} , and other components, indicating the complexity of the fluid properties and the influence of hydrothermal events on early hydrocarbon charging (oil starts to crack gradually at temperatures above $120\text{ }^\circ\text{C}$) [53,54] (Figure 8).

5. Discussion

5.1. Origin of Scapolite

Scapolite comprises a group of volatile-rich, calcium, sodium, aluminum, tectosilicate minerals that includes two endmembers, marialite ($\text{Na}_4\text{Al}_3\text{Si}_9\text{O}_{24}\text{Cl}$) (Ma) and meionite ($\text{Ca}_4\text{Al}_6\text{Si}_6\text{O}_{24}\text{CO}_3$) (Me). In addition, scapolite is the product of high-temperature gas metasomatism of plagioclase in mafic protoliths (the components of precursor basalt is replaced by albite; Figures 5d and 6a,b), and storage for most of the early (high temperature) volatiles (such as Cl, CO_2 , and SO_3). The wide stability range that characterizes scapolite and the presence of a variety of important volatile components make it a good indicator of mineralizing fluid components [55–57]. Scapolite can be altered into epidote, albite, zeolite, and mica through hydrothermal action. During the later low-temperature period or through pressure reduction, the sulfuric volatile components released can form pyrite. However, F^- , Cl^- can enter the mineral or escape along fractures [58–60]. In the Jianyang area, the secondary tourmaline and anthophyllite that occur in the lower basalt section constitute pneumatolytic hydrothermal minerals rich in volatile components such as B, OH^- , and F^- . Tourmaline and anthophyllite can indicate high-temperature magma–hydrothermal and medium-high metamorphic environments, revealing a temperature range of $650\text{ }^\circ\text{C}$ [61]. The emergence of scapolite in the volcanoclastic rocks and secondary tourmaline and anthophyllite in the lower basalt indicates a higher ambient temperature on the one hand, and the presence of a large number of volatiles on the other hand [62,63]. In other words, their occurrence and later evolution not only provide evidence for hydrothermal events after the higher temperature magmatic period of volcanic rocks, but also provide a research basis for studying the influence of the post-magmatic process on volcanoclastic reservoirs in this area. More specifically, the occurrence of scapolite may represent evaporite sequences, and the morphology of evaporites can be greatly changed or even completely changed [64–67]. This is consistent with previous results, which showed that the diagenetic evolution of volcanic minerals is affected by sodium-rich and high-salinity fluids [39].

Microscopic observation and electron probe analysis show that the main mineral components in the lower unaltered basalt are plagioclase (An = 49–57, Ab = 40–48) and augite (Wo = 41–45, En = 31–35, Fs = 19–25), together with ilmenite as an accessory mineral (Figure 7). Considering these minerals and the rock fragments observed in the scapolite, the scapolite is inferred to be the product of the interaction between volatile components in the magmatic gasification–hydrothermal stage and the high-salinity water at the sedimentary stage with the plagioclase in the basal protolith (Figures 5 and 9). In contrast, the microcrystalline titanite was cut by scapolite and occurs in belts; this is readily interpreted as the result of hydration and oxidation of Fe–Ti oxides (ilmenite, Ti-bearing pyroxene, etc.) during the post-magmatic alteration stage. The replacement by sodium-rich hydrothermal fluids led to a large loss of calcium within plagioclase, and the lost calcium was involved in the generation of titanite [39,68]. In addition, the main calcium-rich minerals in the volcanoclastic rocks are titanite ($\text{CaTi}[\text{SiO}_4]$ (O, OH, Cl, F)) rather than calcite (CaCO_3). It is implied that in addition to CO_2 – NaCl – H_2O , there may be an exogenous SiO_2 input into the alteration system before and after the formation of the scapolite.

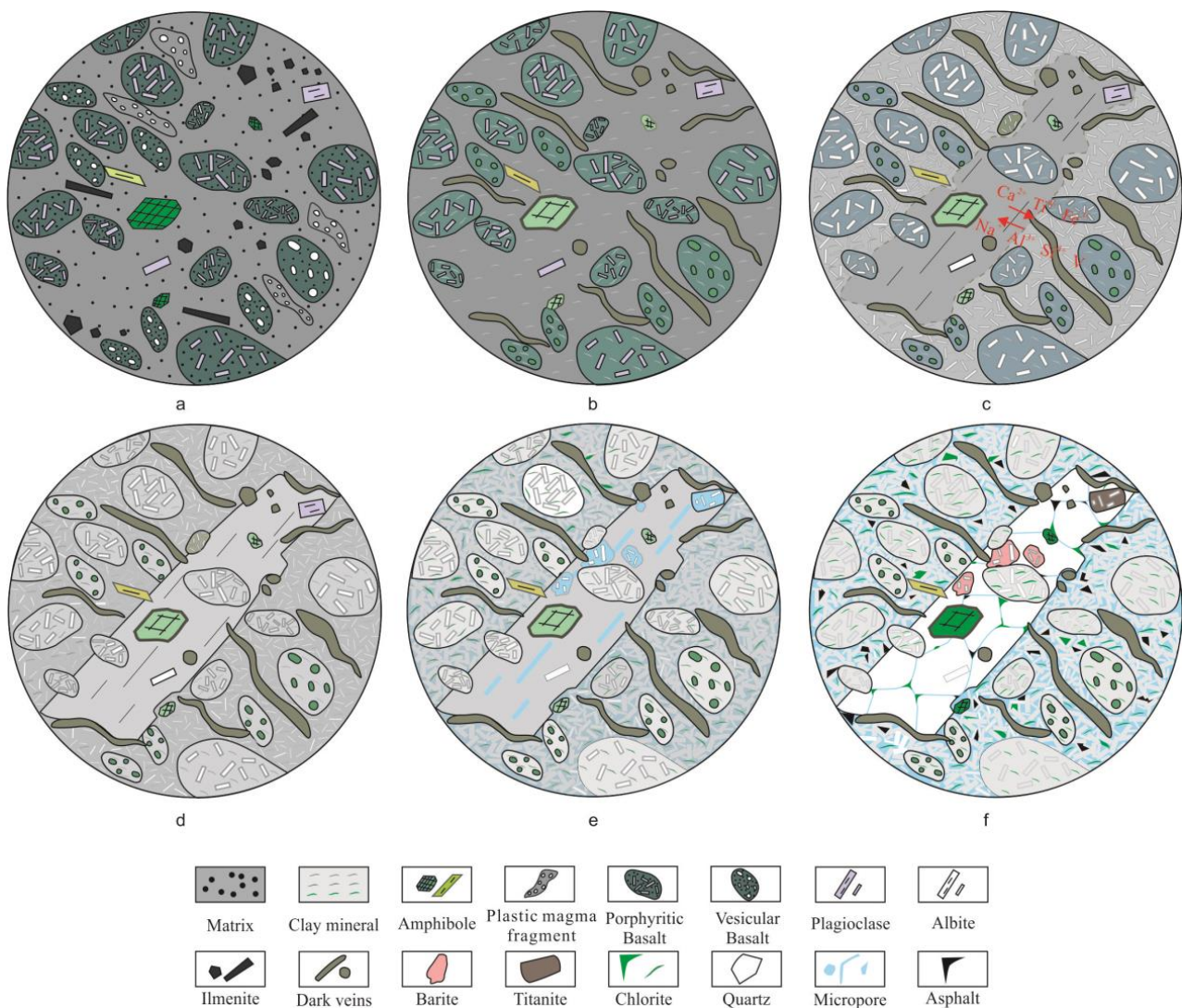


Figure 9. Conceptual model of the formation and evolution of SMMPs in the Permian volcanic rocks in the Jianyang area. (a) Volcanic material formed; (b) Early mineral alteration; (c) Scapolite formation; (d) Scapolite euhedral crystal; (e) Scapolite dissolved along cleavage; (f) Pseudomorph metasomatic scapolite.

5.2. Evolution of Scapolite and Alteration Environments

The quartz occurring as a pseudomorph of scapolite should be the product of alteration by secondary hydrothermal fluids, while the halite and barite in the pores are suggested to be products of Cl and SO₃ volatile components released via the alteration of scapolite, and the combination of Na⁺ and Ba²⁺, respectively. Because the content of barium in seawater is much lower than that of strontium, when affected by meteoric water, Ba²⁺ in meteoric water and SO₄²⁻ in seawater are more prone to precipitating BaSO₄ [69,70]. In addition, the presence of hematite related to weathering in the Permian volcanoclastic rocks [71] indicates that the high content of Ba and barites in rocks may be related to the mixing of meteoric water and sodium-rich hydrothermal fluids [72].

The homogenization temperature and salinity analysis results of the quartz fluid inclusions show that high-temperature–low-salinity magmatic hydrothermal fluid will continue to react with scapolite after its formation [73]. In the quartz fluid inclusions, a large number of hydrocarbons were detected, suggesting that the time the scapolite underwent alteration is consistent with the expulsion of mature hydrocarbons from the

Cambrian-interval source rock [54]. The scapolite was affected by hydrothermal fluid and atmospheric meteoric water after its formation, as revealed by its petrography (Figure 10).

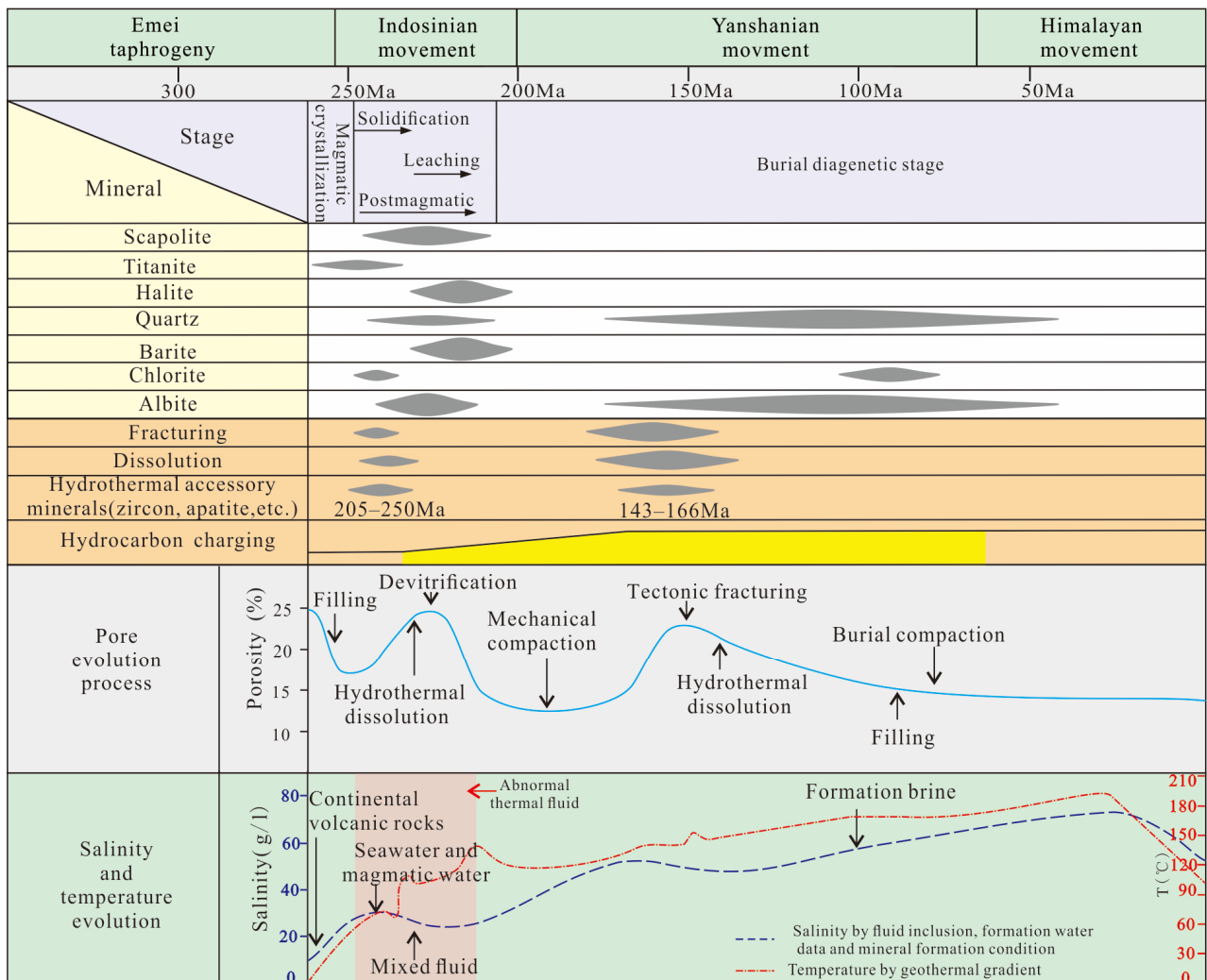
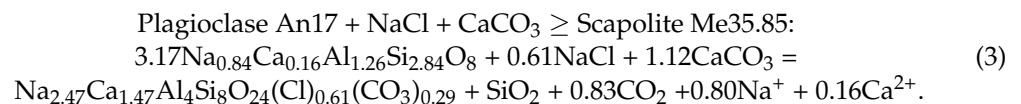


Figure 10. Paragenetic sequence of hydrothermal minerals in Permian volcanoclastic rocks.

Possible reactions of scapolite, titanite, quartz, and other minerals follow:



As mentioned above, there may have been input from allochthon SiO_2 in the system when the scapolite was formed. The input of allochthon SiO_2 fluids not only causes the formation of calcium-rich silicate minerals such as titanite, but also a large number of hydrothermal zircons in the alkaline volcanoclastic rocks [47]. Radiochronometric analyses results for hydrothermal zircon reveal that the Jianyang area has undergone two phases of hydrothermal events related to magmatic action, corresponding to the Indosinian movement during the Early and Middle Triassic (260–225 Ma) and the Yanshanian movement during the Late Jurassic (158.0 ± 0.54 Ma), respectively. Furthermore, the first phases of the event were accompanied by episodic hydrocarbon charging and the formation of

microcrystalline titanite, scapolite, and quartz. In addition, the second-phase hydrothermal event was mainly manifest in the reservoir space [46,74,75].

Since these events, the upper section of the Permian volcanoclastic rocks near the fault zone in the Jianyang area has undergone multistage and multisource hydrothermal fluid alteration. During volcanic eruptions, the volcanoclastic rocks were mainly influenced by sodium-rich and high-salinity seawater. During the solidification period, volcanoclastic rocks were comprehensively affected by (1) the volatiles released via pressure reduction during the ascent of alkaline magma, (2) the deep high-temperature hydrothermal fluid that formed bottom to top along the fault, (3) the charging by hydrocarbon fluids released from maturing Lower Cambrian source rocks, and (4) the circulation of atmospheric meteoric water. In the late diagenesis stage, the rocks were altered by deep hydrothermal fluids and hydrocarbon circulations.

Therefore, the silicification of scapolite and hydrothermal dissolution and albitization of sodium-rich matrix minerals increased the overall pore volume. These processes are beneficial to entry by hydrothermal fluids in later stages. In addition, volcanoclastic reservoirs with micropores (Figure 6) as the main reservoir space were formed by multistage and multisource hydrothermal fluid alteration.

6. Conclusions

(1) Scapolite minerals are present in Permian volcanoclastic rocks in the Jianyang area (SW China) and formed after the microcrystalline titanite; they are products of plagioclase in the mafic protolith altered by high-temperature pneumatolytic metasomatism during the post-magmatic period.

(2) The scapolite was altered by multiple episodes of hydrothermal fluids and finally transformed into quartz and albite, retaining only the precursor pseudomorphs. Halite and barite in the pores are intimately associated with the alteration of scapolite. The precipitation of barite depends on the mixing of meteoric water and barium-rich hydrothermal fluids.

(3) The silicification of scapolite and hydrothermal dissolution of sodium-rich matrix minerals increase the pore volume, which enhances the later entry by hydrothermal fluids. In terms of volcanoclastic reservoirs in hydrocarbon exploration, the common presence of micropores is ascribed to multistage and multisource hydrothermal fluid alteration.

(4) In areas with strong metasomatic alteration, restoration of the protolith based on petrological and mineralogical indicators can provide decisive evidence for further research on volcanoclastic rocks.

Author Contributions: Conceptualization, X.L. and Y.L.; methodology, X.L.; software, Z.C.; validation, X.L. and M.F.; formal analysis, X.L.; investigation, Y.L.; resources, J.C.; data curation, C.T.; writing—original draft preparation, X.L.; writing—review and editing, Y.L.; visualization, H.J.; supervision, M.F.; project administration, M.X.; funding acquisition, X.L. All authors have read and agreed to the published version of the manuscript.

Funding: This research was funded by the National Natural Science Foundation of China (NSFC), “Mechanism of Multiple Authigenic Mineral Symbiosis in Volcanic Reservoirs and Implications for Fluid Tracing” (Grant No. 41202109); National Science and Technology Major Project, “Study of Permian and Triassic Tectonics, Sedimentary Evolution and Reservoir Formation Mechanism in Sichuan Basin” (Grant No. 2016ZX05007004-001); the Major Science and Technology Projects of PetroChina, “Study on main controlling factors of natural gas enrichment in deep clastic and volcanic rocks in Sichuan Basin”. (Grant No. 2021DJ0204) and the Fundamental and Forward-looking Major Science and Technology Project of the PetroChina Company, Limited. “Study on Formation Evolution and Dynamic Mechanism of Middle-Lower Combination in Superposition Basin” (Grant No. 2023ZZ0201).

Data Availability Statement: Data that support the findings of this study are available from the corresponding author upon reasonable request.

Acknowledgments: The manuscript was much improved by the careful reviews of three anonymous reviewers.

Conflicts of Interest: Cong Tan, Zhenglin Cao, Hui Jin, and Maolong Xia are employees of PetroChina. The paper reflects the views of the scientists and not the company.

References

1. Grynberg, M.E.; Papava, D.; Shengelia, M.; Takaishvili, A.; Nanadze, A.; Patton, D.K. Petrophysical characteristics of the middle eocene laumontite tuff reservoir, samgori field, republic of georgia. *J. Pet. Geol.* **1993**, *16*, 313–322. [[CrossRef](#)]
2. Kalan, T.; Sitorus, H.P.; Eman, M. Jatibarang Field, geologic study of volcanic reservoir for horizontal well proposal. In *Indonesia Petroleum Association 23rd Annual Convention*; Indonesian Petroleum Association (IPA): Jakarta, Indonesia, 1994; Volume 1, pp. 229–244. [[CrossRef](#)]
3. Zou, C.N.; Zhao, W.Z.; Jia, C.Z.; Zhu, R.K.; Zhang, G.Y.; Zhao, X.; Yuan, X.J. Formation and distribution of volcanic hydrocarbon reservoirs in sedimentary basins of China. *Pet. Explor. Dev.* **2008**, *35*, 257–271. (In Chinese with English Abstract) [[CrossRef](#)]
4. Ma, X.H.; Yang, Y.; Zhang, J.; Xie, J.R. A major discovery in Permian volcanic rock gas reservoir exploration in the Sichuan Basin and its implications—ScienceDirect. *Nat. Gas Ind. B* **2019**, *6*, 419–425. [[CrossRef](#)]
5. Ma, J.; Huang, Z.; Liang, S.; Liu, Z.; Liang, H. Geochemical and Tight Reservoir Characteristics of Sedimentary Organic-Matter-Bearing Tuff from the Permian Tiaohu Formation in the Santanghu Basin, Northwest China. *Mar. Pet. Geol.* **2016**, *73*, 405–418. [[CrossRef](#)]
6. Zhang, J.; Yu, H.; Kang, S.B.; Cho, J.H.; Min, G.; Stetsenko, V.Y. Effect of Fine-Grained Structural Al–12%Si Materials on Morphologies and Crystal Defects of Eutectic Si in HCC Al–12%Si Alloy Billets. *J. Alloys Compd.* **2012**, *541*, 157–162. [[CrossRef](#)]
7. Pola, A.; Crosta, G.; Fusi, N.; Barberini, V.; Norini, G. Influence of alteration on physical properties of volcanic rocks. *Tectonophysics* **2012**, *566–567*, 67–86. [[CrossRef](#)]
8. Ma, J.; Liu, G.; Huang, Z.; Ou, G.; Li, T.; Guo, X. Tight Tuff Reservoir Characteristics and Its Controlling Factors: A Comparative Study of the Permian Tiaohu Formation and Carboniferous Haerjiawu Formation in the Santanghu Basin, NW China. *J. Pet. Sci. Eng.* **2020**, *187*, 106808. [[CrossRef](#)]
9. Zhu, S.F.; Zhu, X.M.; Liu, X.C.; Li, C.; Wang, X.X.; Tan, M.X.; Geng, M.Y.; Li, Y.P. Alteration products of volcanic materials and their influence on reservoir space in hydrocarbon reservoirs: Evidence from Lower Permian strata in Ke-Xia region, Junggar Basin. *Acta Pet. Sin.* **2014**, *35*, 276–285. (In Chinese with English Abstract)
10. Fulignati, P. Clay Minerals in Hydrothermal Systems. *Minerals* **2020**, *10*, 919. [[CrossRef](#)]
11. Heap, M.J.; Gravley, D.M.; Kennedy, B.M.; Gilg, H.A.; Bertollett, E.; Barker, S.L.L. Quantifying the Role of Hydrothermal Alteration in Creating Geothermal and Epithermal Mineral Resources: The Ohakuri Ignimbrite (Taupō Volcanic Zone, New Zealand). *J. Volcanol. Geotherm. Res.* **2020**, *390*, 106703. [[CrossRef](#)]
12. Pandarinath, K.; Dulski, P.; Torres-Alvarado, I.S.; Verma, S.P. Element Mobility during the Hydrothermal Alteration of Rhyolitic Rocks of the Los Azufres Geothermal Field, Mexico. *Geothermics* **2008**, *37*, 53–72. [[CrossRef](#)]
13. Su, Z.K.; Zhao, X.F.; Wang, C.Y.; Zhu, Z.M.; Song, W.L.; Spandler, C. Survival of Whole-Rock Sm–Nd Isotope System from REE Redistribution and Mineral-Scale Isotopic Resetting amid Hydrothermal Alteration in REE-Rich Fe–Cu Deposit. *Geochim. Et Cosmochim. Acta* **2023**, *348*, 9–26. [[CrossRef](#)]
14. Yuguchi, T.; Hatsukawa, H.; Suzuki, S.; Imura, T.; Motai, S.; Nakashima, K.; Nishiyama, T. Morphological and Chemical Characterization of Secondary Carbonates in the Toki Granite, Central Japan, and the Evolution of Fluid Chemistry. *Am. Miner.* **2022**, *107*, 2282–2290. [[CrossRef](#)]
15. Zhou, P.; Han, X.; Wang, Y.; Wu, X.; Zong, T.; Yu, X.; Liu, J.; Li, H.; Qiu, Z. Hydrothermal Alteration of Basalts in the Ultramafic-Associated Tianxiu Vent Field, Carlsberg Ridge. *Mar. Geol.* **2023**, *463*, 107113. [[CrossRef](#)]
16. Schenato, F.; Formoso, M.L.L.; Dudoignon, P.; Meunier, A.; Proust, D.; Mas, A. Alteration Processes of a Thick Basaltic Lava Flow of the Paraná Basin (Brazil): Petrographic and Mineralogical Studies. *J. S. Am. Earth Sci.* **2003**, *16*, 423–444. [[CrossRef](#)]
17. Diniz, A.C.; de Melo, G.H.C.; de Lana, C.C.; Queiroga, G.N.; de Castro, M.P.; Reis, H.L.S. Unravelling Magmatic-Hydrothermal Processes at Salobo and GT-46 IOCG Deposits, Carajás Mineral Province, Brazil: Constraints from Whole-Rock Geochemistry and Trace Elements in Apatite. *J. South Am. Earth Sci.* **2023**, *125*, 104290. [[CrossRef](#)]
18. Nouri, T.; Tehrani, P.N.; Masoumi, R.; Christidis, G.E. Rare Earth Element Geochemistry of Altered Pyroclastic Rocks in the Hashtjin Area of North-West Iran. *Clay Miner.* **2020**, *55*, 150–165. [[CrossRef](#)]
19. Booden, M.A.; Mauk, J.L. Host Rock Volume Change during Alteration Promotes Self-Sealing of Hydrothermal Systems. In *Proceedings of the Let'S Talk Ore Deposits, Vols I and II*; Barra, F., Reich, M., Campos, E., Tornos, F., Eds.; Ediciones Univ Catolica Norte: Antofagasta, Chile, 2011; pp. 37–39.
20. Li, C.; Shen, P.; Li, P.; Sun, J.; Feng, H.; Pan, H. Changes in the Factors Controlling the Chlorite Composition and Their Influence on Hydrothermal Deposit Studies: A Case Study from Hongguleng Manto-Type Cu Deposit. *J. Geochem. Explor.* **2022**, *243*, 107096. [[CrossRef](#)]
21. Zhong, G.M.; Zhao, X.Y.; Shi, L.; Zhao, M.F.; Sun, N.; Wu, L.; Cai, X.; Xia, W.; Yu, T. Characteristics and main controlling factors of volcanic clastic rock reservoir of Huoshiling Formation in Chaganhua Sub-depression, Changling fault depression of Southern Songliao Basin. *Nat. Gas Geosci.* **2023**, *35*, 84–95. (In Chinese with English Abstract)

22. He, Q.L.; Chen, X.; Ran, Q.; Lv, W.Z.; Chen, K.; Huang, T.J. Seismic-reflection characteristics and lithofacies-distribution prediction of Permian volcanic rocks, Chengdu-Jiayang area. *Nat. Gas Explor. Dev.* **2019**, *42*, 35–41. (In Chinese with English Abstract)
23. Liu, R.; Zhu, B.; Qiu, N.S.; Li, Y.; Wang, W.; Pei, S.Q. New volcanoclastic architectures in the Chengdu-Jiayang Area of the Emeishan Large Igneous Province: Identification, interpretations for the generation mechanism, and estimation on their petroleum reservoir effects. *Earth Sci. Front.* **2023**, 1–17. [[CrossRef](#)]
24. Zhang, W.B.; Li, Y.; Yang, T.; Peng, S.Q.; Cai, L.X.; Ren, Q.Q. Reservoir characteristics and diagenetic evolution of Permian pyroclastic rocks in Jiayang area, Sichuan Basin. *Lithol. Reserv.* **2023**, *36*, 1–11.
25. Liu, X.; Xia, M.L.; Wu, Y.Y.; He, Q.L.; Li, Y.; Liu, R. Characteristics of Permian Volcanoclastic lava reservoirs in Yongtan 1 well, Sichuan Basin. *Nat. Gas Explor. Dev.* **2019**, *42*, 28–36.
26. Somarin, A.K.; Lentz, D.R. Mineralogy, Geochemistry and Fluid Evolution of a Fossil Hydrothermal System in the Paleogene Mendejin Volcanic Sequence, East Azarbaijan, Iran. *Miner. Petrol.* **2008**, *94*, 123–143. [[CrossRef](#)]
27. Shimizu, T.; Manaka, M.; Kazahaya, K.; Tsukamoto, H. Petrographic and Mineralogical Study of Hydrothermal Alteration of the Rokko Granite at Hakusui-Kyo and Horai-Kyo along the Arima-Takatsuki Tectonic Line in Western Japan. *Isl. Arc.* **2021**, *30*, e12407. [[CrossRef](#)]
28. Kawamoto, T. Distribution and Alteration of the Volcanic Reservoir in the Minami-Nagaoka Gas Field. *Sekiyu Gijutsu Kyokaiishi* **2001**, *66*, 46–55. [[CrossRef](#)]
29. Tomaru, H.; Lu, Z.; Fehn, U.; Muramatsu, Y. Origin of hydrocarbons in the Green Tuff region of Japan: 129I results from oil field brines and hot springs in the Akita and Niigata Basins. *Chem. Geol.* **2009**, *264*, 221–231. [[CrossRef](#)]
30. Zhang, L.Y.; Ji, Y.L.; Liu, L.; Zhang, G.; Zhao, L.; Mu, H.Y. Origin of anomalously high porosity in pyroclastic reservoirs: A case study on the northern region of the east sub-sag in Nanbeier sag. *Acta Pet. Sin.* **2012**, *33*, 621–814. (In Chinese with English Abstract)
31. Blazek, M.C. Classification of Pseudomorphs. *Rocks Miner.* **1979**, *54*, 194–197. [[CrossRef](#)]
32. Kar, A.; McEldrew, M.; Stout, R.F.; Mays, B.E.; Khair, A.; Velegol, D.; Gorski, C.A. Self-Generated Electrokinetic Fluid Flows during Pseudomorphic Mineral Replacement Reactions. *Langmuir* **2016**, *32*, 5233–5240. [[CrossRef](#)] [[PubMed](#)]
33. Liu, H.; Ma, T.; Tan, X.; Zeng, W.; Hu, G.; Xiao, D.; Luo, B.; Shan, S.; Su, C. Origin of structurally controlled hydrothermal dolomite in epigenetic karst system during shallow burial: An example from Middle Permian Maokou Formation, central Sichuan Basin, SW China. *Pet. Explor. Dev.* **2016**, *43*, 1000–1012. [[CrossRef](#)]
34. Ma, Y.S.; Guo, X.S.; Guo, T.L.; Huang, R.; Cai, X.Y.; Li, G.X. The Puguang gas field: New giant discovery in the mature Sichuan Basin, southwest China. *Aapg Bull.* **2007**, *91*, 627–643. [[CrossRef](#)]
35. Song, G.Y.; Liu, S.G.; Huang, W.M.; Wang, G.Z.; Chen, C.H.; Ma, W.X.; Zhang, C.J. Characteristics of hydrothermal dolomite of upper Sinian Dengying Formation in the dingshan-lintanchang structural zone, Sichuan Basin, China. *Chengdu Univ. Technol. Sci. Technol. Ed.* **2009**, *36*, 706–715. (In Chinese with English Abstract)
36. Chen, Z.Q. Gas exploration in Sinian Dengying Formation, Sichuan Basin. *China Pet. Explor.* **2010**, *15*, 1–14. (In Chinese with English Abstract)
37. Guo, Z.W.; Deng, K.L.; Han, Y.H. *Formation and Evolution of Sichuan Basin*; Geological Publishing House: Beijing, China, 1996; p. 200. (In Chinese)
38. Pan, J.T.; Liu, H.H.; Yuan, Y.S.; Zhao, J.B.; Zhang, H.H. Late Permian Xuanwei Formation tuff from the western margin of the Upper Yangtze: Constraints on volcanic activity and Paleotethyanarc volcanism in the Emeishan Large igneous Province. *Acta Geol. Sin.* **2022**, *96*, 1985–2000. (In Chinese with English Abstract)
39. Liu, X.H.; Zhuo, Y.Q.; Feng, M.Y.; Zhang, B.; Xia, M.; Wang, X.Z. Constrains of eruption environment and hydrothermal fluid on the Permian pyroclastic reservoirs in the Sichuan Basin, SW China. *Petroleum* **2022**, *8*, 17–30. [[CrossRef](#)]
40. Shellnutt, J.G.; Pham, T.T.; Denyszyn, S.W.; Yeh, M.W.; Tran, T.A. Magmatic Duration of the Emeishan Large Igneous Province: Insight from Northern Vietnam. *Geology* **2020**, *48*, 457–461. [[CrossRef](#)]
41. Ma, X.H.; Li, G.; Ying, D.L.; Zhang, B.J.; Li, Y.; Dai, X.; Fan, Y.X.; Zeng, Y. Distribution and gas-bearing properties of Permian igneous rocks in Sichuan Basin, SW China. *Pet. Explor. Dev.* **2019**, *46*, 228–237. [[CrossRef](#)]
42. Peng, H.; Yin, C.; He, Q.; Xia, G.; Liu, Y.; Ma, T.; Chen, K.; Liu, R.; Su, W. Development Characteristics and Petroleum Geological Significance of Permian Pyroclastic Flow Volcanic Rocks in Western Sichuan Basin, SW China. *Pet. Explor. Dev.* **2022**, *49*, 64–77. [[CrossRef](#)]
43. Wen, L.; Li, Y.; Yi, H.Y.; Liu, X.; Zhang, B.J.; Qiu, Y.C.; Zhou, G.; Zhang, X.H. Lithofacies and reservoir characteristics of Permian volcanic rocks in the Sichuan Basin. *Nat. Gas Ind.* **2019**, *39*, 17–27. (In Chinese with English Abstract) [[CrossRef](#)]
44. Luo, B.; Xia, M.L.; Wang, H.; Fan, Y.; Xu, L.; Liu, R.; Zhan, W.Y. Hydrocarbon accumulation conditions of Permian volcanic gas reservoirs in the western Sichuan Basin. *Nat. Gas Ind.* **2019**, *39*, 9–16. (In Chinese with English Abstract)
45. Zhang, B.Y. Deep Fault System and Its Controlling on the Distribution of Permian Volcanic Rocks in Southwestern Sichuan Basin. Master's Thesis, China University of Geosciences (Beijing), Beijing, China, 2020; pp. 1–105. (In Chinese with English Abstract)
46. Zhuo, Y.Q. Main Controlling Factors of the Permian Volcanoclastic Reservoir of Well YT1 in Jiayang Area, Sichuan Basin. Master's Thesis, Southwest Petroleum University, Chengdu, China, 2022. (In Chinese with English Abstract)
47. Liu, X.H.; Wang, W.W.; Feng, M.Y.; Zhuo, Y.Q.; Yue, H.H. Hydrothermal Process and Duration of Carboniferous Altered Tuff Reservoir in Well Dixi 14 Area of Kelameili Gas Field (Junggar Basin), NW China. *Earth Sci.* **2022**, *47*, 1694–1710. (In Chinese with English Abstract)

48. Rowe, M.C.; Ellis, B.S.; Lindeberg, A. Quantifying Crystallization and Devitrification of Rhyolites by Means of X-ray Diffraction and Electron Microprobe Analysis. *Am. Mineral.* **2012**, *97*, 1685–1699. [[CrossRef](#)]
49. Large, R.R.; Gemmill, J.B.; Paulick, H.; Huston, D.L. The Alteration Box Plot: A Simple Approach to Understanding the Relationship between Alteration Mineralogy and Litho-geochemistry Associated with Volcanic-Hosted Massive Sulfide Deposits. *Econ. Geol.* **2001**, *96*, 957–971. [[CrossRef](#)]
50. Nesbitt, H.W.; Young, G.M. Early Proterozoic Climates and Plate Motions Inferred from Major Element Chemistry of Lutites. *Nature* **1982**, *299*, 715–717. [[CrossRef](#)]
51. Cathelineau, M.; Nieva, D. A Chlorite Solid Solution Geothermometer the Los Azufres (Mexico) Geothermal System. *Contr. Miner. Petrol.* **1985**, *91*, 235–244. [[CrossRef](#)]
52. Bodnar, R.J. Revised equation and table for determining the freezing point depression of H₂O-NaCl solutions. *Geochim. Cosmochim. Acta* **1993**, *57*, 683–684. [[CrossRef](#)]
53. Zhang, N.; Mao, G.J.; Wang, H.T.; Wei, C.Y.; Tuo, Q.; Liu, J.X. Raman spectroscopic characteristics of macromolecular hydrocarbons and its significance in the study of hydrocarbon inclusions. *Geochimica* **2010**, *39*, 345–353. (In Chinese with English Abstract)
54. Wang, W.; Zhao, L.Z.; Zhang, B.J.; Liu, R.; Li, Y.; Zhao, L.K.; Pei, S.Q.; Hu, T. Bitumen development and natural gas enrichment in volcanic reservoirs: A case study of Permian volcanic rocks in the western Sichuan Depression. *J. China Univ. Min.* **2021**, *50*, 1169–1180. (In Chinese with English Abstract)
55. Ellis, D.E. Stability and phase equilibria of chloride and carbonate bearing scapolites at 750 °C and 4000 bar. *Geochim. Cosmochim. Acta* **1978**, *42*, 1271–1281. [[CrossRef](#)]
56. Pan, Y.; Fleet, M.E.; Ray, G.E. Scapolite in Two Canadian Gold Deposits; Nickel Plate, British Columbia and Hemlo, Ontario. *Can. Miner.* **1994**, *32*, 825–837.
57. Almeida, K.; Jenkins, D.M. A Comparison between the Stability Fields of a Cl-Rich Scapolite and the End-Member Marialite. *Am. Miner.* **2019**, *104*, 1788–1799. [[CrossRef](#)]
58. Teertstra, D.K.; Sherriff, B.L. Substitutional Mechanisms, Compositional Trends and the End-Member Formulae of Scapolite. *Chem. Geol.* **1997**, *136*, 233–260. [[CrossRef](#)]
59. Kullerud, K.; Erambert, M. Cl-Scapolite, Cl-Amphibole, and Plagioclase Equilibria in Ductile Shear Zones at Nusfjord, Lofoten, Norway: Implications for Fluid Compositional Evolution during Fluid-Mineral Interaction in the Deep Crust. *Geochim. Cosmochim. Acta* **1999**, *63*, 3829–3844. [[CrossRef](#)]
60. Ren, L.D.; Gao, Y. The role of volatiles in the formation of scapolite in amphibolites of southern West Kunlun Mountains. *Acta Petrologica Et Mineral.* **2002**, *21*, 398–406. (In Chinese with English Abstract)
61. Li, Z.Z.; Qing, K.Z.; Pei, B.; Zhao, J.X.; Shi, R.Z.; Zhao, Z.Z.; Han, R. Mineralogical features of tourmaline in Baiyinchagan Sn-Ag-Pb-Zn deposit, southern Great Xing'an Range, and its implications for magmatic-hydrothermal evolution. *Acta Petrol. Sinica* **2020**, *36*, 3797–3812. [[CrossRef](#)]
62. Comodi, P.; Mellini, M.; Zanazzi, P.F. Scapolites: Variation of Structure with Pressure and Possible Role in the Storage of Fluids. *Eur. J. Miner.* **2019**, *2*, 195–202. [[CrossRef](#)]
63. Kassoli-Fournaraki, A. Ca-Rich Scapolite in Quartz Amphibolites from the Sarti Area, Northern Greece. *Eur. J. Miner.* **1991**, *3*, 887–894. [[CrossRef](#)]
64. Jiang, S.Y.; Palmer, M.R.; Peng, Q.M.; Yang, J.H. Chemical and Stable Isotopic Compositions of Proterozoic Metamorphosed Evaporites and Associated Tourmalines from the Houxianyu Borate Deposit, Eastern Liaoning, China. *Chem. Geol.* **1997**, *135*, 189–211. [[CrossRef](#)]
65. Parnell, J.; Boyce, A.J.; Næraa, T. Seawater Signatures in the Supracrustal Lewisian Complex, Scotland. *Geol. Mag.* **2022**, *159*, 1638–1646. [[CrossRef](#)]
66. Xu, H.; Jin, J.F. Meta-evaporite and Signification in Paleoproterozoic Terrene in Eastern Liaoning Province. *World Geol.* **2001**, *20*, 124–132. (In Chinese with English Abstract)
67. Qiu, Z.; Fan, H.R.; Tomkins, A.; Brugger, J.; Etschmann, B.; Liu, X.; Xing, Y.; Hu, Y. Insights into Salty Metamorphic Fluid Evolution from Scapolite in the Trans-North China Orogen: Implication for Ore Genesis. *Geochim. Cosmochim. Acta* **2021**, *293*, 256–276. [[CrossRef](#)]
68. Hou, M.C.; Deng, M.; Zhang, B.J.; Wang, W.; Li, X.H.; Wang, W.K.; Pei, S.Q.; Yang, Y. A major Ti-bearing mineral in Emeishan basalts: The occurrence, characters and genesis of sphene. *Acta Petrol. Sin.* **2011**, *27*, 2487–2499. (In Chinese with English Abstract)
69. Wang, A.H. Discriminant effect of sedimentary environment by the Sr/Ba ratio of different existing forms. *Acta Sedimentol. Sin.* **1996**, *14*, 169–174. (In Chinese with English Abstract)
70. Qian, Y.X.; Chen, Y.; Ma, H.Q.; Chen, Q.L. Chemical Analysis and Origin of Calcite Filled in and Cave with in Ordovician Carbonates in Tahe Oilfield, Xinjiang. *Acta Sedimentol. Sin.* **2004**, *22*, 6–12. (In Chinese with English Abstract)
71. Hou, M.C.; Wang, W.K.; Zhang, B.J.; Wang, W.; Li, X.H.; Deng, M.; Pei, S.Q.; Yang, Y. Fluid types and activities of Emeishan basalt in Zhougong mountain-Hanwang field of Sichuan Province. *Acta Petrol. Sin.* **2013**, *29*, 2709–2718. (In Chinese with English Abstract)
72. Kribek, B.; Hladikova, J.; Fryda, J. Scapolite- and Anhydrite-Bearing Rocks from the Moldanubian Zone of the Bohemian Massif: Metamorphosed Exhalites and Evaporites. *J. Geosci.* **1997**, *42*, 62.
73. Zeng, Q.F. The polygenetic hydrothermal metallogeny. *Sci. Geol. Sin.* **1985**, *2*, 145–153. (In Chinese with English Abstract)

74. Feng, M.Y.; Shang, J.X.; Shen, A.J.; Wen, L.; Wang, X.Z.; Xu, L.; Liang, F.; Liu, X.H. Composite episodic hydrothermal alteration on the Middle Permian carbonate reservoirs and its geological significance in southwestern Sichuan Basin, SW China. *Pet. Explor. Dev.* **2024**, *51*, 1–14. (In Chinese with English Abstract) [[CrossRef](#)]
75. Tan, J.; Zhou, K.M.; Zeng, L.; Zou, C.Y.; Yan, Y.X.; Kong, L.M.; Yuan, X.L. Quantitative analysis method for crystalline and amorphous components in volcanic rocks: A case study on Permian volcanic rocks in the western Sichuan Basin. *Nat. Gas Ind.* **2022**, *42*, 24–33. (In Chinese with English Abstract)

Disclaimer/Publisher’s Note: The statements, opinions and data contained in all publications are solely those of the individual author(s) and contributor(s) and not of MDPI and/or the editor(s). MDPI and/or the editor(s) disclaim responsibility for any injury to people or property resulting from any ideas, methods, instructions or products referred to in the content.